Check for updates

Tunable Negative and Positive Photoconductance in Van Der Waals Heterostructure for Image Preprocessing

Zhaotan Gao, Ruiqi Jiang, Menghan Deng, Can Zhao, Zian Hong, Liyan Shang, Yawei Li, Liangqing Zhu, Jinzhong Zhang, Jian Zhang, and Zhigao Hu**

The processing of visual information occurs mainly in the retina, and the retinal preprocessing function greatly improves the transmission quality and efficiency of visual information. The artificial retina system provides a promising path to efficient image processing. Here, graphene/InSe/*h*-BN heterogeneous structure is proposed, which exhibits negative and positive photoconductance (NPC and PPC) effects by altering the strength of a single wavelength laser. Moreover, a modified theoretical model is presented based on the power-dependent photoconductivity effect of laser: $I_{ph} = -mP^{\alpha_1} + nP^{\alpha_2}$, which can reveal the internal physical mechanism of negative/positive photoconductance effects. The present 2D structure design allows the field effect transistor (FET) to exhibit excellent photoelectric performance ($R_{NPC} = 1.1\times 10^4$ AW^{-1}, $R_{PPC} = 13$ AW^{-1}) and performance stability. Especially, the retinal pretreatment process is successfully simulated based on the negative and positive photoconductive effects. Moreover, the pulse signal input improves the device responsivity by 167%, and the transmission quality and efficiency of the visual signal can also be enhanced. This work provides a new design idea and direction for the construction of artificial vision, and lay a foundation for the integration of the next generation of optoelectronic devices.

1. Introduction

In recent years, deep network-based learning methods have achieved remarkable success with the rapid development of artificial intelligence.[1] Therefore, achieving interaction and perception with the real world becomes the primary problem to be solved. For humans, more than 80% of information comes from vision. The retina, as the primary visual organ, converts light signals into electrical signals.[2–4] Compared to traditional vision chips, the retina can simultaneously perceive and preprocess visual information. This greatly improves the transmission quality and transmission efficiency of visual information.[5,6] Therefore, building a perception system with pre-processing function is a prerequisite for artificial vision to obtain information efficiently. Through the preprocessing function of the sensing system, redundant visual data is discarded and optical information can be efficiently extracted.[7,8]

Inspired by the above concept, bidirectional tunable optoelectronic devices are gradually developed. Traditional optoelectronic devices realize high-efficiency sensing and wide-band detection of optical signals, while they cannot take into account the preprocessing function of optical signals.[9,10] In order to achieve bidirectional modulation of optoelectronic devices in sensing signals, Kim et al. developed an artificial vision system with adaptive functions.[11] By adjusting the load transistor in the peripheral circuit, the perception behavior of the environment under different light intensity has been successfully realized. Although photoelectric hybrid modulation provides greater freedom for the construction of artificial vision systems, the increase in peripheral circuits makes circuit design and manufacturing processes more complex, and is not conducive to the integrated development of future devices.[12] Compared to the two-terminal devices, the three-terminal structure allows the devices to achieve bidirectional modulation of signals by taking advantage of the adjustable gate.[6,13,14] Due to bandwidth-connection-density trade-offs and interconnection problems, signal processing speed is limited.[15,16] Therefore, bidirectional light modulation is necessary. Recently, some researchers have developed laser wavelength-dependent bidirectional modulation. The devices exhibit both negative and

Z. Gao, R. Jiang, M. Deng, C. Zhao, Z. Hong, L. Shang, Y. Li, L. Zhu, J. Zhang, Z. Hu
Technical Center for Multifunctional Magneto-Optical Spectroscopy (Shanghai)
Engineering Research Center of Nanophotonics & Advanced Instrument (Ministry of Education)
Department of Physics
School of Physics and Electronic Science
East China Normal University
Shanghai 200241, China
E-mail: jzzhang@ee.ecnu.edu.cn; zghu@ee.ecnu.edu.cn

J. Zhang
School of Communication and Electronic Engineering
East China Normal University
Shanghai 200241, China

Z. Hu
Collaborative Innovation Center of Extreme Optics
Shanxi University
Taiyuan, Shanxi 030006, China

The ORCID identification number(s) for the author(s) of this article can be found under https://doi.org/10.1002/adma.202401585

DOI: 10.1002/adma.202401585

© 2024 Wiley-VCH GmbH

positive photoconductance (NPC and PPC) effects by inputting different specific laser wavelength.[15,17–21] This structural design makes the devices free from the bondage of electrical signal, and realizes true all-optical modulation, which makes it more suitable for the construction of artificial vision systems. While significant progress has been made, a number of challenges and shortcomings have been still remained. The bidirectional optical modulation caused by specific wavelengths greatly limits the application scenarios of all-optical devices. In addition, wavelength-dependent all-optical modulation devices cannot achieve synchronous modulation in time. Therefore, it is of great significance to develop bidirectional optical modulators under the same wavelength light. According to photoelectric effect theory, light intensity is another key factor to affect photocurrent.[22] Cai et al. constructed a fully photocontrolled retinal morphometric memristor based on halide perovskite materials. The NPC effect at low light intensity could improve image clarity and recognition of images.[23] However, research on similar phenomena in the field of 2D layered materials is relatively limited.

Since the advent of graphene in 2004, it has been widely used in the research of optoelectronic devices due to its ultra-high carrier concentration, high Fermi level efficiency and wide band photoelectric response characteristics.[24] In 2010, Levesque et al. systematically studied the influence of the atmosphere on the doping effect of graphene, showing that graphene can achieve *p*-type doping under atmospheric conditions.[25] Subsequently, Yang et al. applied the Bi_2O_2Se-graphene hybrid structure to a neuromorphic device to control its positive and negative photoresponse by stimulating light of different wavelengths to achieve long-term potentiation or long-term depression under light stimulation.[21] In 2023, Liang et al. realized all-optical control of artificial synapses based on graphene/titanium dioxide (TiO_2) quantum dot heterostructure, and its conductivity could be enhanced and inhibited at 635 and 365 nm, respectively.[17] As a typical III-VI layered material, InSe has a smaller effective electron mass ($m^* = 0.14\,m_0$) than MoS_2 ($m^* = 0.45\,m_0$), which make it exhibit high mobility over 10^3 $cm^2\,V^{-1}\,s^{-1}$ at room temperature,[26] and a low electron-hole recombination makes it exhibit a high photoresponse.[27] Lei et al. achieved tunable ambipolar photoresponsivity by constructing WSe_2/InSe heterostructure with photogating effect, which can exhibit a very high photoresponse (-1.76×10^4, 5.48×10^4 AW^{-1}).[28] Shang et al. designed a self-powered photodetector with photoinduced electric field enhancement based on 2D InSe/WSe_2/SnS_2 van der Waals heterojunction, and its responsivity is a 50 times increase compared to the InSe/WSe_2 photodetector.[29] Although optoelectronic devices based on graphene and other material systems have made some progress in the research of reversible photoresponse, most of them need to rely on a variety of specific bands of light sources. This greatly limits the application scenarios of all-optical regulation. Therefore, we are eager to propose a new idea of regulation: negative and positive photoconductance effects depend on laser power density, so as to remove the dependence of reversible light response regulation on the laser band.

In this study, we propose a field effect transistor (FET) based on the graphene/InSe/*h*-BN heterostructure to realize the conversion of negative and positive photoconductance effects by applying a single wavelength laser. It exhibits excellent optical performance ($R_{NPC} = 1.1\times 10^4$ AW^{-1}, $R_{PPC} = 13$ AW^{-1}) and device stability. The pulse signal input under the PPC effect causes the dark current of graphene/InSe/*h*-BN heterojunction-based FETs to decrease, while the photocurrent level increases. The pulse signal input increases the device's responsiveness by 167%. Based on the NPC and PPC effects controlled by laser power density, a modified theoretical model is proposed and extended to the full optical modulation range. Bidirectional modulation of NPC and PPC effects has been successfully applied to retinal preprocessing of visual signals. This research shows that 2D heterostructures have great application prospects in integrated optoelectronic devices and single-light bidirectional modulation.

2. Results and Discussion

2.1. Structural Characterization

Figure 1a and Figure S1a (Supporting Information) show a 3D diagram and an optical microscopic image of a graphene/InSe/*h*-BN heterojunction based FET, respectively. In this structure, graphene acts as a conductive channel, InSe acts as a light absorbing layer and *h*-BN is used as the interface contact layer to improve the interface contact between InSe/SiO_2 and graphene/SiO_2.[30,31] As monitored from AFM images and the line profiles (Figure S1, Supporting Information), the average thicknesses of graphene, InSe and *h*-BN flakes are about 4, 9.5, and 12 nm, respectively. In Figure 1b, a clear and flat interface indicates that there is good contact between the layers. For graphene, InSe and *h*-BN, lattice fringes are clearly observed, which indicates that they have a high crystal quality. In Figure 1c, the EDS element mapping shows the top-down distribution of C, Se, and N elements, corresponding to graphene, InSe and *h*-BN, respectively. The high crystal quality of graphene, InSe and *h*-BN flakes prepared by mechanical stripping was confirmed by Raman spectroscopy (Figures S2a and S2b, Supporting Information).

In order to analyze the interface effect between graphene and InSe, the surface potentials in separate and contact states are measured by a KPFM system. The contact potential difference (CPD) between the tip and sample is measured by applying voltage to the tip, and the work function of the sample is calculated according to the formula: $V_{CPD} = (\phi_{tip} - \phi_{sample}) / e$, where ϕ_{tip} is the work function of the tip, ϕ_{sample} is the work function of the sample, and e is the elementary charge.[32] In the separated state, the work functions of graphene and InSe are 5 and 5.5 eV, respectively, as shown in Figure 1d, Figures S2d and S2e (Supporting Information). It suggests that graphene shows *p*-type property in the isolated state. In order to analyze the reasons, the work function before and after contact with air was compared. The Fermi level of graphene decreases by 0.1−−0.2 eV after 2 h in air (Figure S3, Supporting Information). The KPFM test results of graphene/InSe and InSe/graphene heterojunctions show that when graphene is contacted with InSe, the surface potential of graphene decreases while the surface potential of InSe increases. Therefore, when graphene forms a heterojunction with InSe, the energy band of InSe bends downward due to the mismatch between the work functions, as shown in Figure 1d and Figure S4 (Supporting Information).[33]

To explore the photoelectric performance of graphene/InSe/*h*-BN heterojunction based FETs, the basic electrical properties of

© 2024 Wiley-VCH GmbH

15214095, 2024, 29, Downloaded from https://onlinelibrary.wiley.com/doi/10.1002/adma.202401585 by East China Normal University, Wiley Online Library on [30/08/2024]. See the Terms and Conditions (https://onlinelibrary.wiley.com/terms-and-conditions) on Wiley Online Library for rules of use; OA articles are governed by the applicable Creative Commons License

15214095, 2024, 29, Downloaded from https://onlinelibrary.wiley.com/doi/10.1002/adma.202401585 by East China Normal University, Wiley Online Library on [30/08/2024]. See the Terms and Conditions (https://onlinelibrary.wiley.com/terms-and-conditions) on Wiley Online Library for rules of use; OA articles are governed by the applicable Creative Commons License

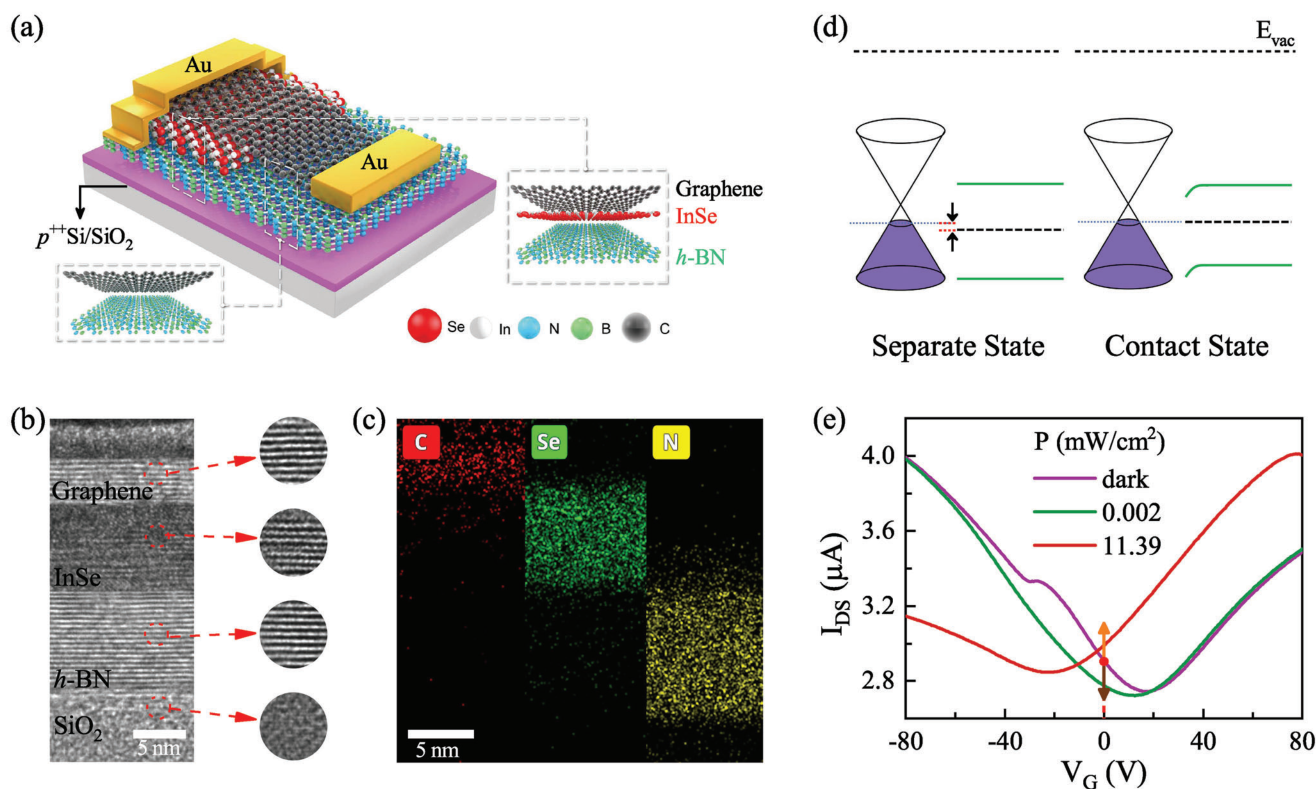

Figure 1. Characterization of a FET based on graphene/InSe/*h*-BN heterojunction. a) 3D schematic diagram of the device composing of graphene, InSe, and *h*-BN layers. b) Cross-section TEM images of the heterogeneous structure and c) the corresponding EDS element mapping. d) Band structures of graphene and InSe in separate and contact state, respectively. e) Transfer characteristic curves of the graphene/InSe/*h*-BN heterojunction FET under different laser power densities; $\lambda = 405$ nm, $V_{DS} = 0.01$ V.

InSe, graphene and graphene/InSe/*h*-BN heterojunction FETs were investigated (Figure S5, Supporting Information). It shows that the FETs have good ohmic contact with Au electrodes, and both the graphene and the graphene/InSe/*h*-BN FET exhibit weak *p*-type doping characteristics under dark conditions, which is consistent with KPFM results. Comparing the output and transfer characteristic curves of the three types of FETs, graphene is the main conductive layer in graphene/InSe/*h*-BN heterojunction FETs. The photoresponse of the graphene/InSe/*h*-BN heterojunction FET were studied by measuring the transfer characteristic curves at the wavelength of 405 nm, as shown in Figure 1e. It shows that the graphene/InSe/*h*-BN heterojunction FET exhibits opposite photoresponse characteristics by applying the laser with different intensities (V_G = 0V), macroscopically manifested as an increase (P = 11.39 mWcm^{-2}) and decrease (P = 0.002 mWcm^{-2}) in current levels under light conditions (compared to dark current levels). The negative and positive photoconductance effects dependent on laser power densities can be achieved by graphene/InSe/*h*-BN heterojunction FETs.

2.2. Negative and Positive Photoconductance Effects of Laser Power Density Modulation

During the photoelectric test, the laser is incident perpendicular to the surface of the device and can cover the entire channel uniformly, as shown in **Figure** 2a. In order to further investigate the positive and negative photoconductance effects of graphene/InSe/*h*-BN heterojunction FETs, the photoresponse characteristics of the graphene/InSe/*h*-BN FET under single pulse (wavelength: 405 nm, pulse width: 1 s) conditions are tested, as shown in Figure 2b,c. When P $\leqslant$ 0.098 mWcm^{-2}, the FET exhibits a NPC effect. At this time, the current level under light is lower than the initial current level. With increasing the laser power density, the NPC effect becomes more obvious. It shows that the NPC of graphene/InSe/*h*-BN heterojunction FETs can accept laser power modulation, which agrees with the general physical law. With the further increase of laser power density, the NPC effect gradually decreases. For the case of 0.098<P<5.12 mWcm^{-2}, although the FET still exhibits a NPC effect, the increasing laser power density weakens the current variation. Note that following the cessation of light in this laser power range, the current level drops to a position equivalent to that observed when the laser power density reaches 0.098 mWcm^{-2}. For the case of P $\geqslant$ 5.12 mWcm^{-2}, the FET exhibits a PPC effect, and the current level under light conditions increases rapidly. Note that the current level of the FET will still drop below the initial current level instantaneously after the light is turned off, which is differs from the traditional photoresponse. In addition, after the stopping of illumination (P $\geq$ 5.12 mWcm^{-2}), the device current level increases with the increase of the laser power density. When the pulsed laser power density is less than

 © 2024 Wiley-VCH GmbH

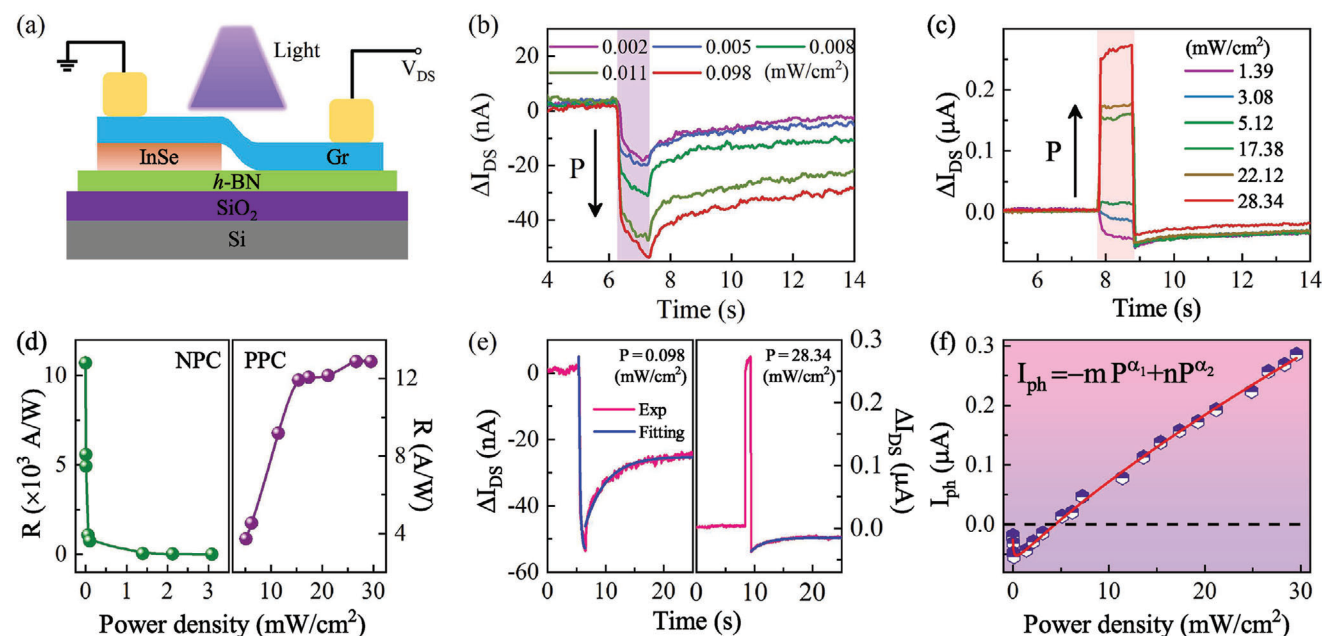

Figure 2. Photoelectric properties of the FET based on graphene/InSe/*h*-BN heterostructure. a) Structure diagram of a graphene/InSe/*h*-BN heterostructure FET under light. b) NPC effect and c) negative and positive photoconductance effects conversion process with increasing laser power density, $\Delta I_{DS} = I_1 - I_0$, I_0 represents the initial dark current level, $V_{DS} = 0.1V$. d) Responsivity and e) time-response characteristics of the FET under two photoconductive effects. f) Experimental and fitted photocurrent as a function of laser power density.

28.34 mWcm^{-2}, the current level will gradually recover from the initial current level with time. The photoresponse curves at different laser power densities show that the graphene/InSe/*h*-BN heterojunction-based FET can achieve NPC and PPC effects modulated by laser power density. At the same time, according to the feature of photoresponse characteristic curves, the transformation process of PPC and NPC effects can be divided into three stages during the increase of laser power density: 1) Enhancement stage of NPC effect; 2) Attenuation stage of NPC effect; 3) Enhancement stage of PPC effect. Note that full contact of InSe and graphene will suppress the photoresponse performance compared to the device structure where InSe only partially contacts the channel graphene (Figure S6, Supporting Information). In addition, the similar phenomenon has been observed by applying 637 nm light laser (Figure S7, Supporting Information). Fortunately, the opposite conversion process from PPC to NPC are also realized (Figure S8, Supporting Information). In Figure S8 (Supporting Information), a pulse signal with a high laser power density (P = 23.6 mWcm^{-2}) causes the graphene/InSe/*h*-BN heterojunction-based FET to exhibit a positive photoresponse. The current level of the device gradually recovers with time after the laser is turned off. The device displays a negative photoresponse by applying a pulse signal with a laser power density of 0.001 mWcm^{-2}. The graphene/InSe/*h*-BN heterojunction-based FET can realize the conversion from PPC to NPC effect under time conditions. Based on the above mechanism analysis, we propose two methods to reset the condition for the initial state of the device. (Figure S9, Supporting Information). In Figure S9a (Supporting Information), a long pulse interval can restore the photocurrent level after NPC effect to the initial state and let the graphene/InSe/*h*-BN heterojunction-based FET show NPC effect again during the second laser (P = 0.001 mWcm^{-2}). We can also reset the device state with the gate voltage pulses. Figure S9b (Supporting Information) shows that under the condition of low laser power density (P = 0.001 mWcm^{-2}), the current level of the device shows a negative optical response and does not return to the initial state in a short time after illumination. Fortunately, a forward gate pulse can make the current level of the device quickly return to the initial state for another negative photoresponse. Its initial state can be reset by waiting a recovery time or applying a gate pulsed voltage to exhibit negative light response again. Note that it is convenient in practical applications to reset the device by applying a single pulsed gate voltage. Therefore, there is a physical process of laser power dependence in the conversion process of negative and positive photoconductance effects. It is the existence of this physical process that divides the entire modulation process into the above three stages, which will be described in detail in part C. It means that graphene/InSe/*h*-BN heterojunction FETs have the potential to tunable positive and negative photoconductance effects at a single wavelength.

As a new type of photoelectric device, in addition to its unusual physics, another concern is its performance. As one of the physical quantities used to measure the detection efficiency of photoelectric devices, the responsivity is calculated by the following formula:[21] $R = |I_{ph}|/(PS)$, where $I_{ph} = I_{light} - I_{dark}$, P is the laser power density, S is the effective area of transistor. When the FET exhibits a NPC effect, the responsivity gradually decreases with increasing the laser power density, and finally tends to saturation. A high responsivity of up to 1.1×10^4 AW^{-1} based on NPC effect is achieved, which is better than most reported photoelectric devices.[21,34,35] With the further increase of laser power density, the FET begins to show a PPC effect, the responsivity increases

 © 2024 Wiley-VCH GmbH

15214095, 2024, 29, Downloaded from https://onlinelibrary.wiley.com/doi/10.1002/adma.202401585 by East China Normal University, Wiley Online Library on [30/08/2024]. See the Terms and Conditions (https://onlinelibrary.wiley.com/terms-and-conditions) on Wiley Online Library for rules of use; OA articles are governed by the applicable Creative Commons License

with increasing the laser power density, and tends to saturation at the detected laser power density. The reversal trend of the responsivity further indicates the conversion of the photoconductive effect. Figure 2e shows the time-response characteristics of the device under negative and positive photoconductance effects, respectively. The current drop/recovery process under NPC effect and the current recovery process under PPC effect are fitted and analyzed based on the Kohlrausch law:[16] $I(t) = I_0 + A exp[(-t)/\tau]$, I_0, A, and τ represent the stable current, the fitting factor and the characteristic relaxation time, respectively. For the negative photoresponse process, the characteristic relaxation time of the current drop/recovery is 0.21 and 3.60 s, respectively. When the FET transforms into a PPC effect, the characteristic relaxation time of the recovery process is 2.49 s. In Figure S10 (Supporting Information), the heterojunction FET maintains a good negative and positive photoresponse under continuous cycle test conditions. Comparing the levels of photocurrent in different cycles, with only 9% and 18% fluctuation relative to the photocurrent average level.

In order to further analyze the relationship between negative/positive photoconductance effects and laser power density, the photocurrent is plotted as a function of laser intensity (Figure 2f). The relationship between the photocurrent and incident laser power density is explained by the modified power-law formula:

$$I_{ph} = -mP^{\alpha_1} + nP^{\alpha_2} \tag{1}$$

where m and n are fitting factors, α_1 and α_2 are power factors. The ideal value of α is 1, while electron-hole recombination and carrier capture cause α to be less than 1.[27,36] Since there are two photoconductive effects, a double power function is used for fitting. Among them, the fitting factors m and n are 90 and 43.6, respectively, and the fitted power factors were $\alpha_1 = 0.2$ and $\alpha_2 = 0.69$, respectively. It means that the device photocurrent is mainly dominated by the former at $P \leq 0.098$ mWcm^{-2}. $\alpha_1 = 0.2$ indicates that a large number of electron-hole recombination or photogenerated charges are trapped at low laser power density. With increasing the laser power density, the proportion of the latter term gradually increases, and the NPC effect gradually decreases. This is consistent with what has been observed experimentally. For the case of $P \geqslant 5.12$ mWcm^{-2}, the photocurrent of the device is mainly dominated by the latter term. The $\alpha_2 = 0.69$ indicates that the recombination effect of electron-hole pairs gradually decreases or the fraction of the trapped photogenerated charge decreases at high laser power density. The fitting results indicate that the modified power-law formula can perfectly match the experimental results, and reveal the internal physical process of negative and positive photoconductance effects dependent on laser power density.

2.3. Mechanisms of NPC and PPC of Laser Power Modulation

In order to further investigate the effect of laser power density on photoconductivity, the photoresponse curves under the condition of double pulses were tested. **Figure 3a** shows the photoswitching characteristics of the graphene/InSe/h-BN heterojunction FET at three laser power densities under the dual pulse condition ($V_{DS} = 0.1$ V, $\lambda = 405$ nm, pulse width: 1 s and pulse period: 2 s). When the first pulse is applied, the photoconductive effect of the device is modulated by the laser power density, the photoconductive effect is negative or positive. At the end of the first laser pulse, the current at the three different laser powers are below the initial dark current level. Since the consumed holes in the graphene have not been fully recovered, with the application of a second light pulse, the device exhibits a PPC effect at power densities of 3.08 and 19.3 mWcm^{-2}. It suggests that the continuous light pulse not only reduces the current level of the device, but also realizes the conversion of the photoconductive effect. In other words, FETs based on graphene/InSe/h-BN heterojunction have a memory function. This phenomenon is obvious in the multi-pulse condition where the laser power density gradually increases (Figure S11, Supporting Information). With the increase of power density and time, the photoconductive effect is transformed due to the fact that the higher incident light power density induces more photo-generated carrier production. When the device changes from NPC effect to PPC effect, with the increasing power density of pulsed laser, the photocurrent level continues to increase while the dark current level of the device continues to decrease until it reaches a stable state. This result further proves that the photoconductive effect of graphene/InSe/h-BN heterojunction FETs is dependent on the laser power density. Note that the change in dark current observed in Figure S11 (Supporting Information) differs from that shown in Figures 2c and 3a since the partial consumption of wholes in graphene. In Figure 3b, the Dirac voltage (V_D) of graphene under dark conditions is 17 V. It is p-type doping caused by air (Figure S3, Supporting Information).[25] When light is applied to the device, the V_D of graphene gradually shifts to a lower level, indicating that electron photodoping of graphene causes the initial p-type doping effect to weaken.[15,37] When $P > 0.09$ mWcm^{-2}, the V_D begins to move in the direction of -V_G, which proves that graphene shifts from the initial p-type doping to n-type doping at this power density. The position of V_D moves upward as it shifts to the left due to the increase of photogenerated electrons under high power density illumination. Based on the change of graphene Dirac voltage at different power densities, the work function of graphene at the corresponding laser power density was plotted in Figure 3c and the insert shows the Dirac voltage as a function of laser power density.[38] The work function of graphene in the graphene/InSe/h-BN heterojunction before illumination is larger than that of intrinsic graphene (red), which indicates the p-type doping characteristics of graphene in the graphene/InSe/h-BN heterojunction FET. Under light conditions, the work function of graphene gradually decreases, indicating that its p-type doping properties gradually weaken. With the further increase of laser power density, the work function drops below the eigenvalue, which indicates that the increase of laser power density causes the graphene to change from p-type doping to n-type doping. Note that the critical values of laser power density that cause Dirac voltage and doping characteristics to change are consistent with those required for photoconductive effect to change. Based on this analysis, the following mechanism model is proposed.

The mechanism of a negative/positive photoresponse at different light power densities is illustrated in Figure 3d. The work function mismatch between graphene and InSe causes the InSe

© 2024 Wiley-VCH GmbH

15214095, 2024, 29, Downloaded from https://onlinelibrary.wiley.com/doi/10.1002/adma.202401585 by East China Normal University, Wiley Online Library on [30/08/2024]. See the Terms and Conditions (https://onlinelibrary.wiley.com/terms-and-conditions) on Wiley Online Library for rules of use; OA articles are governed by the applicable Creative Commons License

15214095, 2024, 29, Downloaded from https://onlinelibrary.wiley.com/doi/10.1002/adma.202401585 by East China Normal University, Wiley Online Library on [30/08/2024]. See the Terms and Conditions (https://onlinelibrary.wiley.com/terms-and-conditions) on Wiley Online Library for rules of use; OA articles are governed by the applicable Creative Commons License

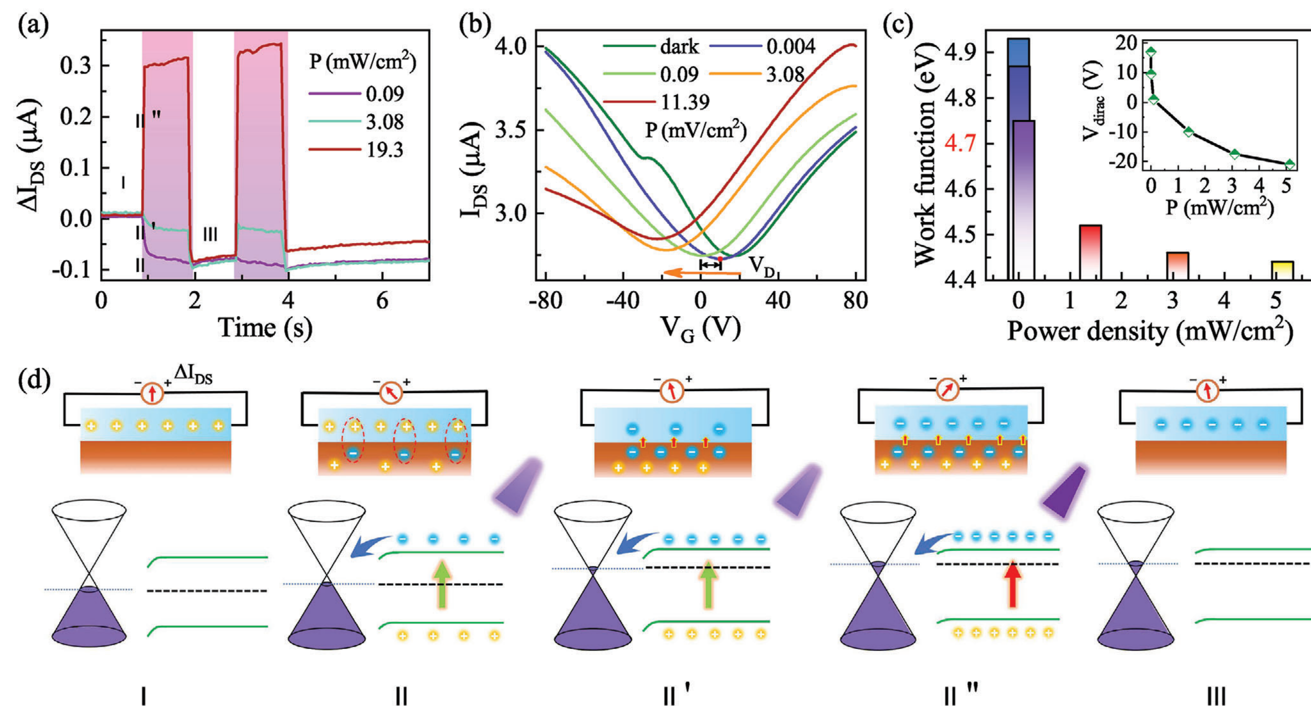

Figure 3. Mechanism diagram of the FET based on graphene/InSe/*h*-BN heterojunction. a) Photoswitching and b) transfer characteristic curves of the FET under different laser power densities, the arrow shows the direction of the Dirac voltage shift. c) Graphene work function as a function of laser power density, Inset: Dirac voltage as a function of the laser power density. d) Schematic diagram and energy band alignment for the graphene/InSe/*h*-BN heterojunction under (I) dark (before illumination), (II) P = 0.09 $mWcm^{-2}$, (II′) P = 3.08 $mWcm^{-2}$, (II″) P = 19.3$mWcm^{-2}$ and (III) dark (after illumination).

band to bend downward at the graphene/InSe interface when forming a heterogeneous structure (Figures 1d and 3d I).[33] The current level at this point is defined as the initial dark current. When P = 0.09 $mWcm^{-2}$, most light is absorbed by InSe and a small number of electron-hole pairs are generated because of the weak light absorption capacity of graphene (only 2.3% in the monolayer graphene sheet).[39] Driven by a built-in electric field between graphene and InSe, photogenerated electrons are transferred into graphene and recombined with holes, resulting in a concentration decrease of charge carriers in graphene. The macroscopic manifestation is the decrease in photocurrent (Figure 3d II). There are two main physical processes in the lighting process: one is that the photogenerated electrons transfer from InSe to graphene by the internal electric field. The other one is that the photogenerated electrons in the graphene layer are combined with the internal holes. In addition, there also exists a separation process of electron-hole pairs in graphene. The photocurrent remains constant when the recombination and separation of electron-hole pairs reach equilibrium under illumination, as shown in Figure S12 (Supporting Information). Note that a part of photogenerated electrons that do not participate in recombination can still participate in the conduction of graphene layers.

Based on the amount of photogenerated electrons in the graphene layer and the amount of recombination, negative, or positive photoconductance effects can be achieved in the macroscopic state. As the holes in graphene are consumed, the *p*-type doping effect is weakened, resulting in a decrease from the work function of graphene and an increase in the Fermi level (Figure 3c,d II). During the second light pulse, the photogenerated electrons generated by the InSe layer continue to be transferred to graphene driven by the built-in electric field to recombine with the holes, resulting in a further decrease of the current level. Compared with the drop level of the first photocurrent, the change in the photocurrent produced by the second illumination is much smaller since the holes consumed in graphene have not been fully recovered.

As the laser power density further increases (P = 3.08 $mWcm^{-2}$), the InSe layer generates more photogenerated electrons, which continue to transfer into the graphene layer, as shown in Figure 3d II′. At this time, it is considered that the amount of transferred photogenerated electrons is slightly more than the holes in the graphene layer, and the recombination speed of electron-hole pairs is greater than the transfer speed of photogenerated electrons. Therefore, light causes the current level of the device to gradually decrease and eventually reach an equilibrium state. At this point, the photogenerated electrons transferred from the InSe layer participate in the conduction of graphene. Therefore, graphene changes from *p*-type to *n*-type doping (Figure 3b,c). After the illumination, the transfer process of photogenerated electrons stops, and the original holes in the graphene layer have not been recovered, resulting in an instant drop in the current level at the moment of stopping light. Since the holes in graphene are completely depleted under the first light pulse and only recover a small amount during the light-stop process, the device exhibits a PPC effect under second illumination.

 © 2024 Wiley-VCH GmbH

When P = 19.3 $mWcm^{-2}$, a large number of photogenerated electrons are produced in the InSe layer, as shown in Figure 3d II″. The holes in the graphene layer are quickly consumed, and the remaining amount of photogenerated electrons is still greater than the initial amount of holes, making the device exhibit a PPC effect. After the holes in graphene are completely exhausted, it can be considered that the physical process at this time only includes the transfer process of photogenerated electrons, and the response time of the device is greatly shortened (Figure 2e). When P = 0.098 and 28.34 $mWcm^{-2}$, the response time of the device is 0.7 and 0.1 s, respectively.

In order to further study the process of photogenerated electron transfer and electron-hole pair recombination, graphene/InSe heterostructure without *h*-BN are investigated.[31,40] Due to the charge capture effect between SiO_2 and InSe, at the same laser intensity, the number of photogenerated electrons transferred from InSe to graphene is reduced. This means that under the same light conditions, the holes in graphene can remain for a longer time.[41] Under constant illumination, the graphene/InSe heterostructure FET can realize the transition from photogenic inhibition to photogenic enhancement. The comparison results of different laser power densities show that the higher the laser power density, the shorter the duration of the negative photoresponse, and the smaller the change of current level in the negative photoresponse stage (Figure S13, Supporting Information). This result further proves the correctness of the above theory of photogenerated charge transfer and electron-hole pair recombination.

In the case of graphene/InSe/*h*-BN heterostructure FETs, light causes holes in graphene to be continuously consumed. Therefore, after stopping illumination, the current level of the FET will drop below the initial dark current level, as shown in Figure 3a III, d III. Before illumination, holes are dopant charges in graphene/InSe/*h*-BN heterostructure FETs, which is caused by air. With the application of light, the concentration of holes in doped graphene gradually decreases. When the laser power density exceeds the critical value (P > 0.09 $mWcm^{-2}$), the main carrier type in graphene changes from hole to electron. At this point, the doping charge in the FET appears as an electron. The electron concentration in doped graphene increases with the increase of laser power density (Figure S14, Supporting Information).[42] This is a doping effect caused by photogenic charge. Note that the critical value of the laser power density that causes the charge doping type transformation in graphene is consistent with the critical value required to change the type of photoconductive effect.

2.4. Self-Noise Reduction of Transmission Signal

Whether it is a creature or a machine, there should be signal transmission in the process of interacting with the outside world. 80% of perceived external stimuli are light information obtained through the visual system. In the process of signal receiving, there is often a part of noise. The noise not only increases the signal transmission pressure, but also interferes with normal signal detection. If the device can pre-process the signal while receiving it, the key information can be selectively optimized from a large amount of raw data, and signal transmission quality can be improved.[7] **Figure 4a** shows the optical signal self-processing process realized by FETs based on graphene/InSe/*h*-BN heterojunction. When the visual signal reaches the visual receptor, the noise is filtered by the NPC effect, and the normal signal can be enhanced under the PPC effect and signal transmission is realized. When the visual signal is re-input, the noise and normal signal are further weakened and enhanced based on the memory effect of the devices. The visual signal can be perceived and transmitted efficiently by this signal processing process.

In the process of vision formation, the retina is the main receiver of light signals, which can be converted into electrical signals. The retinal preconditioning function greatly improves the work efficiency of the cerebral cortex. In order to simulate the preprocessing of optical signals by the retina, four types of laser power densities were first selected as input sources to simulate self-noise reduction processing, and the comparison of output results before and after input and between different input sources were drawn. In Figure 4b, laser power densities corresponding to regions I, II, IV, and V are 0.09, 3.08, 5.12, and 21.18 $mWcm^{-2}$, and normalized values are -0.3, -0.08, 0.9, and 1, respectively. Areas I and II are defined as noise. Areas IV and V are defined as normal signals. Area III corresponds to the dark current level in the initial state (i.e., the state before the signal input). Except for area III, the rest are the states at the time of signal input (the light signal processing process). Here, the ratio is used to quantitatively analyze the enhancement and suppression effects of different signal sources, and the formula is as follows: $C = N_2 / N_1$, where N_1 and N_2 are normalized photocurrents triggered by different signal sources, respectively. The comparison results of the color block area suggest that the noise has been weakened to various degrees (blue box selection area), and the normal signal is perceived and enhanced (orange box selection area). The comparison results between different signal sources show that when the noise and normal signal are 0.09, 21.18 $mWcm^{-2}$, respectively, C = -3.3 (the negative sign means there is light suppression), the enhancement and suppression effects are the most obvious (green box selection area), and the noise reduction processing of visual signals is realized.

In the process of image information recognition, the presence of background (especially similar to the input signal) greatly increases the difficulty of image recognition. Based on the negative/positive photoconductance effects and the memory effect, the preprocessing of visual signals in 2D space is simulated. The two laser intensities (0.09 and 19.3 $mWcm^{-2}$) distributed in 2D space are defined as noise and normal signals, respectively. In Figure 4c, "8" is the input signal, and the rest is the "background", which contains noise. Under the double pulse signals, C is -3.9 and -4, respectively. Compared to conventional photodetectors (N = 0.9), higher quality image signals ($0.9<|-3.9|$) can be obtained through self-noise reduction and signal enhancement processing (Figure S15, Supporting Information).

Figure 4d shows that the second signal input increases the responsivity of the device by 167% (Gain/First pulse) in the image recognition process. Input of double pulse signals reduces the dark current level of the graphene/InSe/*h*-BN heterojunction-based FET. In addition, holes in the graphene layer are further consumed, which increases the photocurrent level of the device. In terms of device stability, 2D layered materials, such as InSe and black phosphorus (BP) are easily subjected to oxidation or

 © 2024 Wiley-VCH GmbH

15214095, 2024, 29, Downloaded from https://onlinelibrary.wiley.com/doi/10.1002/adma.202401585 by East China Normal University, Wiley Online Library on [30/08/2024]. See the Terms and Conditions (https://onlinelibrary.wiley.com/terms-and-conditions) on Wiley Online Library for rules of use; OA articles are governed by the applicable Creative Commons License

15214095, 2024, 29, Downloaded from https://onlinelibrary.wiley.com/doi/10.1002/adma.202401585 by East China Normal University, Wiley Online Library on [30/08/2024]. See the Terms and Conditions (https://onlinelibrary.wiley.com/terms-and-conditions) on Wiley Online Library for rules of use; OA articles are governed by the applicable Creative Commons License

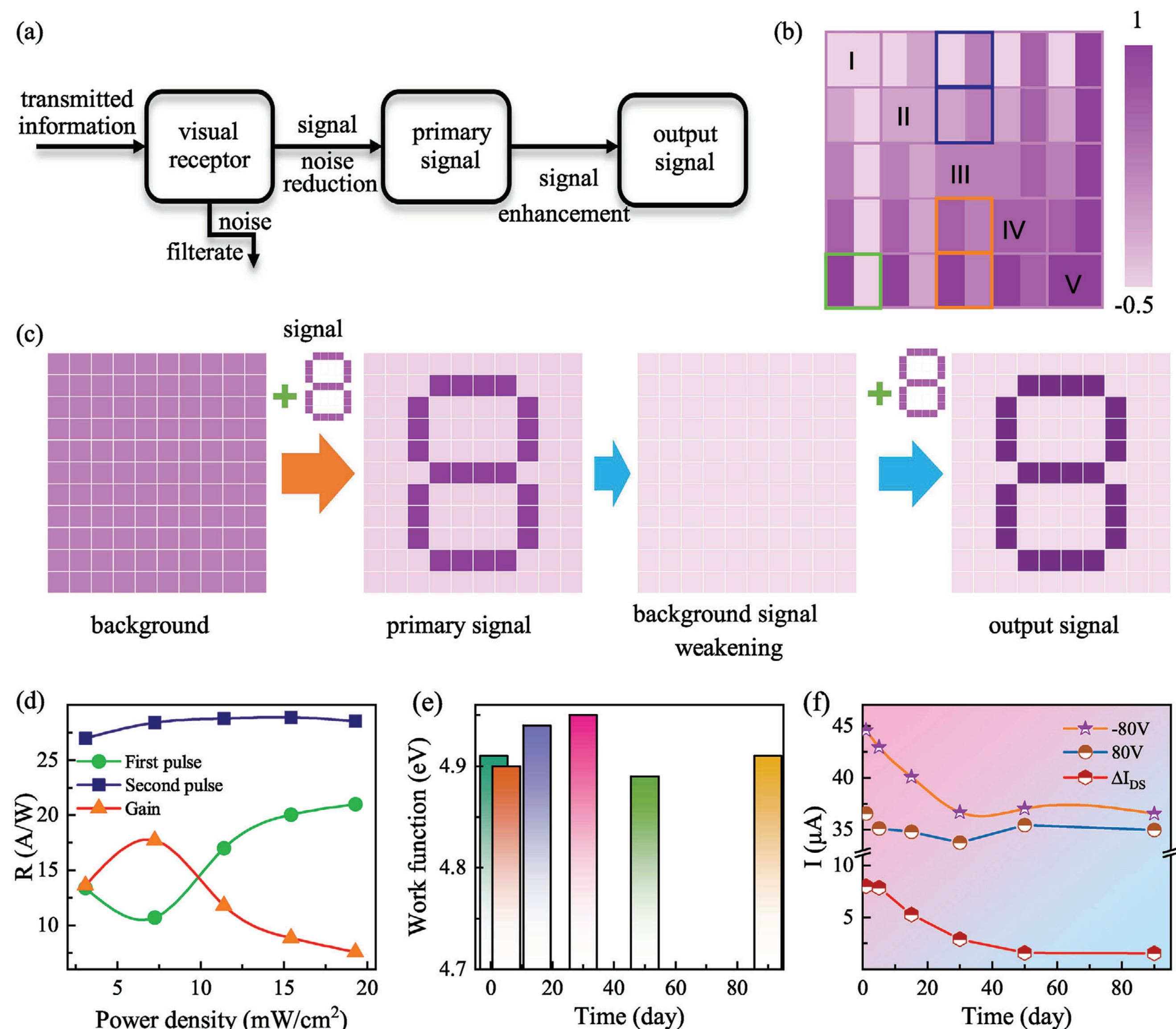

Figure 4. Image self-noise reduction processing based on negative and positive photoconductance effects. a) Signal self-denoising processing model. b) Comparison diagram of photocurrent in noise reduction process of different input light intensities. c) Output image signal enhancement process under double pulse conditions. d) Photoresponsivity and gain of the FET in double pulse process. e) Work function of graphene in graphene/InSe/*h*-BN heterojunction and f) current level of the graphene/InSe/*h*-BN heterostructure FET at room temperature during three months ($V_G = \pm 80\,V$, $\Delta I_{DS} = I_{-80\,V} - I_{+80\,V}$).

other reactions caused by external environmental factors, resulting in poor stability of the prepared device.[43,44] The sandwich structure graphene/InSe/*h*-BN effectively avoids direct contact between InSe and air (Figure S1a, Supporting Information). It allows the device to maintain its original performance at room temperature for more than three months, and the *p*-type doping characteristics and current level of the device are maintained in a constant range, as shown in Figures 4e,f. It indicates that this structure design has obvious advantages in the device stability, which is better than that of InSe/graphene/*h*-BN-based FET due to the protective effect of graphene on InSe (Figures S16 and S17, Supporting Information).[45] Moreover, the graphene/InSe/*h*-BN heterojunction-based FET exhibits a good stable performance of NPC and PPC effects according to the cycle-to-cycle retention statistics tests (Figures S18 and S19, Supporting Information).

3. Conclusion

In summary, we propose a graphene/InSe/*h*-BN heterostructure based FET with the negative and positive photoconductance effects of laser power tuning by a single wavelength with various power densities. Through the pulse signal, the light current increases and the dark current is suppressed, which is attributed to the transfer doping of photogenic charge. Under the illumination, InSe is photoexcited to produce electron-hole pairs, where electrons transfer to *p*-type doping graphene and recombine with

 © 2024 Wiley-VCH GmbH

holes, thereby reducing the macroscopic current level to achieve NPC effect. With the increase of laser power density, a large number of photoelectron-hole pairs are generated. When the transfer amount is greater than the recombination amount, the device exhibits a PPC effect. Under negative and positive photoconductance effects, the device has excellent photoresponse characteristics ($R_{NPC} = 1.1\times 10^4$ AW^{-1}, $R_{PPC} = 13$ AW^{-1}). In a further step, we propose a modified theoretical model ($I_{ph} = -mP^{\alpha_1} + nP^{\alpha_2}$), which can be extended to the full optical modulation range and unify the negative and positive photoconductance effects. Moreover, it has excellent device stability at room temperature. KPFM results reveal the *p*-type doping characteristics of graphene in air and the interface effect between graphene and InSe. When InSe comes into contact with graphene, the energy band of InSe bends downward due to a mismatch between the work functions. This method offers the significant advantage of being able to directly compare surface potentials after contact with each other to determine the direction of Fermi level movement. Finally, the retinal visual signal preprocessing process is successfully simulated based on graphene/InSe/*h*-BN heterojunction FETs. The pulse signal input increases the responsivity of the device by 167%, which greatly improves the transmission quality and transmission efficiency of the visual signal. All the results show that the negative and positive photoconductance effects of laser power density modulation based on graphene/InSe/*h*-BN heterostructure have great application prospects in integrated optoelectronic devices and all-optical modulation.

4. Experimental Section

Device Fabrication: Graphene, InSe, and *h*-BN flakes were obtained from the corresponding bulk crystals (Shanghai Onway Techology Co., Ltd) by mechanical exfoliation, and then were stacked vertically on 285 nm-thick SiO_2/p^{++}_Si substrates in turn by dry transfer. The source and drain of heterojunctions were patterned by a copper mask technique. Thermal evaporation was used for Au (50 nm) electrode deposition.

Device Characterizations: The morphology and thickness of graphene, InSe and *h*-BN flakes and their heterojunctions were characterized by optical microscopy and atomic force microscopy (AFM Dimension Icon, Bruker), respectively. Raman spectra and photoluminescence (PL) spectra were obtained by a confocal micro-Raman spectrometer (Jobin-Yvon LabRAM HR Evolution, Horiba) with the 532 nm-laser. The surface potentials of graphene and InSe were measured by kelvin probe force microscopy system (KPFM Dimension Icon, Bruker). The cross-section of graphene/InSe/*h*-BN heterojunction was obtained by focusing ion beam (FIB, G4 PFIB Hxe, Helios) technique. The TEM image and energy dispersive spectrometer (EDS) elemental mapping of the device were measured by transmission electron microscopy (Talos F200X G2, FEI).

Graphene/InSe/*h*-BN heterojunction based FETs were measured electrically and optically using a Keithley 4200-SCS semiconductor parameter analyzer. All tests of the device were conducted in a vacuum (10^{-6} Torr) and dark environment, and only exposed to the target light source environment. In the photoelectric measurement process, commercial light emitting diodes with illumination wavelengths of 405 and 637 nm were used (Thorlabs, Inc.). The laser spot area was 5 cm^2. A laser diode controller (ITC4001, Thorlabs, Inc.) was used to control the laser to produce light pulses with tunable laser power, pulse width and frequency.

Supporting Information

Supporting Information is available from the Wiley Online Library or from the author.

Acknowledgements

This work was financially supported by the National Natural Science Foundation of China (Grant nos. 62090013, 62074058, and 62375086), the National Key Research and Development Program of China (Grant no. 2019YFB2203403), Projects of Science and Technology Commission of Shanghai Municipality (Grant no. 21JC1402100), the Program for Professor of Special Appointment (Eastern Scholar) at Shanghai Institutions of Higher Learning.

Author Contributions

Z. T. G., C. Z., and Z. A. H. performed the preparation of 2D layered materials and the construction of heterojunctions. Z. T. G., M. H. D., and C. Z. conducted the experiments for device fabrication and electrical measurements. Z. T. G., R. Q. J., M. H. D., L. Y. S., L. Q. Z., Y. W. L., and J. Z. Z. performed the detailed analyses of the underlying mechanism Z. T. G., J. Z. Z., J. Z., and Z. G. H. designed the experiments and wrote the manuscript. J. Z. and Z. G. H. supervised the research. All authors have given approval to the final version of the manuscript.

Conflict of Interest

The authors declare no conflict of interest.

Data Availability Statement

The data that support the findings of this study are available from the corresponding author upon reasonable request.

Keywords

artificial retina simulation, light intensity dependence, negative and positive photoconductance, van der Waals heterostructures

Received: January 30, 2024
Revised: April 15, 2024
Published online: May 9, 2024

[1] S. Ullman, *Science* **2018**, *363*, 692.
[2] L. Gu, S. Poddar, Y. Lin, Z. Long, D. Zhang, Q. Zhang, L. Shu, X. Qiu, M. Kam, A. Javey, Z. Fan, *Nature* **2020**, *581*, 278.
[3] K. Lee, H. Han, Y. Kim, J. Park, S. Jang, H. Lee, S. W. Lee, H. Kim, Y. Kim, T. Kim, D. Kim, G. Wang, C. Park, *Adv. Funct. Mater.* **2021**, *31*, 2105596.
[4] Q. Liu, L. Yin, C. Zhao, J. Wang, Z. Wu, H. Lei, Y. Liu, B. Tian, Z. Zhang, Z. Zhao, R. Liu, C. Ding, Y. Han, C.-Q. Ma, P. Song, I. Z. Mitrovic, E. G. Lim, Z. Wen, *Nano Energy* **2022**, *102*, 107686.
[5] N. Wu, *Sci. China Inf. Sci.* **2018**, *61*, 060421.
[6] C.-Y. Wang, S.-J. Liang, S. Wang, P. Wang, Z. a. Li, Z. Wang, A. Gao, C. Pan, C. Liu, J. Liu, H. Yang, X. Liu, W. Song, C. Wang, B. Cheng, X. Wang, K. Chen, Z. Wang, K. Watanabe, T. Taniguchi, J. J. Yang, F. Miao, *Sci. Adv.* **2020**, *6*, eaba6173.
[7] J. Y. Zhang, P. Guo, Z. Guo, L. Li, T. Sun, D. Liu, L. Tian, G. Zu, L. Xiong, J. H. Zhang, J. Huang, *Adv. Funct. Mater.* **2023**, *33*, 2302885.
[8] X. Shan, C. Zhao, X. Wang, Z. Wang, S. Fu, Y. Lin, T. Zeng, X. Zhao, H. Xu, X. Zhang, Y. Liu, *Adv. Sci.* **2021**, *9*, 2104632.
[9] H. Wang, S. Gao, F. Zhang, F. Meng, Z. Guo, R. Cao, Y. Zeng, J. Zhao, S. Chen, H. Hu, Y. J. Zeng, S. J. Kim, D. Fan, H. Zhang, P. N. Prasad, *Adv. Sci.* **2021**, *8*, 2100503.

© 2024 Wiley-VCH GmbH

15214095, 2024, 29, Downloaded from https://onlinelibrary.wiley.com/doi/10.1002/adma.202401585 by East China Normal University, Wiley Online Library on [30/08/2024]. See the Terms and Conditions (https://onlinelibrary.wiley.com/terms-and-conditions) on Wiley Online Library for rules of use; OA articles are governed by the applicable Creative Commons License

[10] M. Dai, H. Chen, F. Wang, M. Long, H. Shang, Y. Hu, W. Li, C. Ge, J. Zhang, T. Zhai, Y. Fu, P. Hu, *ACS Nano* **2020**, *14*, 9098.
[11] S. M. Kwon, S. W. Cho, M. Kim, J. S. Heo, Y.-H. Kim, S. K. Park, *Adv. Mater.* **2019**, *31*, 1906433.
[12] W. Lu, Q. Chen, H. Zeng, H. Wang, L. Liu, T. Guo, H. Chen, R. Wang, *Nano Res.* **2023**, *16*, 10004.
[13] H. Xiong, L. Xu, C. Gao, Q. Zhang, M. Deng, Q. Wang, J. Zhang, D. Fuchs, W. Li, A. Cui, L. Shang, K. Jiang, Z. Hu, J. Chu, *ACS Appl. Mater. Interfaces* **2021**, *13*, 50132.
[14] D.-C. Hu, R. Yang, L. Jiang, X. Guo, *ACS Appl. Mater. Interfaces* **2018**, *10*, 6463.
[15] Y.-X. Hou, Y. Li, Z.-C. Zhang, J.-Q. Li, D.-H. Qi, X.-D. Chen, J.-J. Wang, B.-W. Yao, M.-X. Yu, T.-B. Lu, J. Zhang, *ACS Nano* **2021**, *15*, 1497.
[16] L. Xu, H. Xiong, Z. Fu, M. Deng, S. Wang, J. Zhang, L. Shang, K. Jiang, Y. Li, L. Zhu, L. He, Z. Hu, J. Chu, *Phys. Rev. Applied* **2021**, *16*, 044049.
[17] J. Liang, X. Yu, J. Qiu, M. Wang, C. Cheng, B. Huang, H. Zhang, R. Chen, W. Pei, H. Chen, *ACS Appl. Mater. Interfaces* **2023**, *15*, 9584.
[18] L. Hu, J. Yang, J. Wang, P. Cheng, L. O. Chua, F. Zhuge, *Adv. Funct. Mater.* **2020**, *31*, 2005582.
[19] R. Ji, G. Feng, C. Jiang, B. Tian, C. Luo, H. Lin, X. Tang, H. Peng, C. G. Duan, *Adv. Electron. Mater.* **2022**, *8*, 2101402.
[20] T. Ahmed, S. Kuriakose, E. L. H. Mayes, R. Ramanathan, V. Bansal, M. Bhaskaran, S. Sriram, S. Walia, *Small* **2019**, *15*, 1900966.
[21] C.-M. Yang, T.-C. Chen, D. Verma, L.-J. Li, B. Liu, W.-H. Chang, C.-S. Lai, *Adv. Funct. Mater.* **2020**, *30*, 2001598.
[22] D. A. Nguyen, S. Cho, S. Park, D. Y. Park, H. C. Suh, M. S. Jeong, T. P. Anh Bach, H. Kim, H. Im, *Nano Energy* **2023**, *113*, 108552.
[23] B. Cai, Y. Huang, L. Tang, T. Wang, C. Wang, Q. Sun, D. W. Zhang, L. Chen, *Adv. Funct. Mater* **2023**, *33*, 2306272.
[24] K. S. Novoselov, A. K. Geim, S. V. Morozov, D. Jiang, Y. Zhang, S. V. Dubonos, I. V. Grigorieva, A. A. Firsov, *Science* **2004**, *306*, 666.
[25] P. L. Levesque, S. S. Sabri, C. M. Aguirre, J. Guillemette, M. Siaj, P. Desjardins, T. Szkopek, R. Martel, *Nano Lett.* **2010**, *11*, 132.
[26] Z. Li, H. Qiao, Z. Guo, X. Ren, Z. Huang, X. Qi, S. C. Dhanabalan, J. S. Ponraj, D. Zhang, J. Li, J. Zhao, J. Zhong, H. Zhang, *Adv. Funct. Mater.* **2018**, *28*, 1705237.
[27] H. Jang, Y. Seok, Y. Choi, S. H. Cho, K. Watanabe, T. Taniguchi, K. Lee, *Adv. Funct. Mater.* **2020**, *31*, 2006788.
[28] T. Lei, H. Tu, W. Lv, H. Ma, J. Wang, R. Hu, Q. Wang, L. Zhang, B. Fang, Z. Liu, W. Shi, Z. Zeng, *ACS Appl. Mater. Interfaces* **2021**, *13*, 50213.
[29] H. Shang, F. Gao, M. Dai, Y. Hu, S. Wang, B. Xu, P. Wang, B. Gao, J. Zhang, P. Hu, *Small Methods* **2023**, *7*, 2200966.
[30] C. Biswas, F. Güneş, D. D. Loc, S. C. Lim, M. S. Jeong, D. Pribat, Y. H. Lee, *Nano Lett.* **2011**, *11*, 4682.
[31] N. Izyumskaya, D. O. Demchenko, S. Das, Ü. Özgür, V. Avrutin, H. Morkoç, *Adv. Electron. Mater.* **2017**, *3*, 1600485.
[32] M. Deng, X. Wang, X. Xu, A. Cui, K. Jiang, J. Zhang, L. Zhu, L. Shang, Y. Li, Z. Hu, J. Chu, *Mater. Horiz.* **2023**, *10*, 1309.
[33] Z. Chen, J. Biscaras, A. Shukla, *Nanoscale* **2015**, *7*, 5981.
[34] Y. Xue, Y. Zhang, Y. Liu, H. Liu, J. Song, J. Sophia, J. Liu, Z. Xu, Q. Xu, Z. Wang, J. Zheng, Y. Liu, S. Li, Q. Bao, *ACS Nano* **2015**, *10*, 573.
[35] H. Jawa, A. Varghese, S. Ghosh, S. Sahoo, Y. Yin, N. V. Medhekar, S. Lodha, *Adv. Funct. Mater.* **2022**, *32*, 2112696.
[36] S. Guo, Z. Chen, D. Weller, X. Wang, C. Ding, Y. Wang, R. Liu, *ACS Appl. Mater. Interfaces* **2021**, *13*, 56438.
[37] C. Han, X. Liu, X. Han, M. He, J. Han, H. Zhang, X. Hou, H. Zhou, H. Yu, Z. Wu, J. Gou, J. Wang, *Adv. Funct. Mater.* **2022**, *32*, 2209680.
[38] T. J. Yoo, S. Y. Kim, M. G. Kwon, C. Kim, K. E. Chang, H. J. Hwang, B. H. Lee, *Laser Photonics Rev.* **2021**, *15*, 2000557.
[39] X. Wang, Z. Cheng, K. Xu, H. K. Tsang, J.-B. Xu, *Nat. Photonics* **2013**, *7*, 888.
[40] L. Liu, L. Wu, A. Wang, H. Liu, R. Ma, K. Wu, J. Chen, Z. Zhou, Y. Tian, H. Yang, C. Shen, L. Bao, Z. Qin, S. T. Pantelides, H.-J. Gao, *Nano Lett.* **2020**, *20*, 6666.
[41] F.-S. Yang, M. Li, M.-P. Lee, I. Y. Ho, J.-Y. Chen, H. Ling, Y. Li, J.-K. Chang, S.-H. Yang, Y.-M. Chang, K.-C. Lee, Y.-C. Chou, C.-H. Ho, W. Li, C.-H. Lien, Y.-F. Lin, *Nat. Commun.* **2020**, *11*, 2972.
[42] W. Hu, Z. Li, J. Yang, *J. Chem. Phys.* **2013**, *138*, 124706.
[43] T.-H. Tsai, F.-S. Yang, P.-H. Ho, Z.-Y. Liang, C.-H. Lien, C.-H. Ho, Y.-F. Lin, P.-W. Chiu, *ACS Appl. Mater. Interfaces* **2019**, *11*, 35969.
[44] J. D. Wood, S. A. Wells, D. Jariwala, K.-S. Chen, E. Cho, V. K. Sangwan, X. Liu, L. J. Lauhon, T. J. Marks, M. C. Hersam, *Nano Lett.* **2014**, *14*, 6964.
[45] Z. Chen, J. Biscaras, A. Shukla, *Nanoscale* **2015**, *7*, 5981.

 © 2024 Wiley-VCH GmbH

15214095, 2024, 29, Downloaded from https://onlinelibrary.wiley.com/doi/10.1002/adma.202401585 by East China Normal University, Wiley Online Library on [30/08/2024]. See the Terms and Conditions (https://onlinelibrary.wiley.com/terms-and-conditions) on Wiley Online Library for rules of use; OA articles are governed by the applicable Creative Commons License